Nonlinear optical diode effect in a magnetic Weyl semimetal

Christian Tzschaschel,[1,*] Jian-Xiang Qiu,[1] Xue-Jian Gao,[2] Hou-Chen Li,[1] Chunyu Guo,[3,4] Hung-Yu Yang,[5] Cheng-Ping Zhang,[2] Ying-Ming Xie,[2] Yu-Fei Liu,[1] Anyuan Gao,[1] Damien Bérubé,[1] Thao Dinh,[1] Sheng-Chin Ho,[1] Yuqiang Fang,[6,7] Fuqiang Huang,[6,7] Johanna Nordlander,[8] Qiong Ma,[5] Fazel Tafti,[5] Philip J.W. Moll,[3,4] Kam Tuen Law,[2] and Su-Yang Xu[1,†]

[1]*Department of Chemistry and Chemical Biology, Harvard University, Massachusetts 02138, USA*

[2]*Department of Physics, Hong Kong University of Science and Technology, Clear Water Bay, Hong Kong, China*

[3]*Laboratory of Quantum Materials (QMAT), Institute of Materials (IMX), École Polytechnique Fédérale de Lausanne (EPFL), CH-1015, Lausanne, Switzerland*

[4]*Max Planck Institute for the Structure and Dynamics of Matter, Hamburg, Germany*

[5]*Department of Physics, Boston College, Chestnut Hill, MA, USA*

[6]*State Key Laboratory of High Performance Ceramics and Superfine Microstructure, Shanghai Institute of Ceramics, Chinese Academy of Science, Shanghai, China*

[7]*State Key Laboratory of Rare Earth Materials Chemistry and Applications, College of Chemistry and Molecular Engineering Peking University, Beijing, China*

[8]*Department of Physics, Harvard University, Massachusetts 02138, USA*

ABSTRACT

Weyl semimetals have emerged as a promising quantum material system to discover novel electrical and optical phenomena, due to their combination of nontrivial quantum geometry and strong symmetry breaking. One crucial class of such novel transport phenomena is the diode effect, which is of great interest for both fundamental physics and modern technologies. In the electrical regime, giant electrical diode effect (the nonreciprocal transport) has been observed in Weyl systems. In the optical regime, novel optical diode effects have been theoretically considered but never probed experimentally. Here, we report the observation of the nonlinear optical diode effect (NODE) in the magnetic Weyl semimetal CeAlSi, where the magnetic state of CeAlSi introduces a pronounced directionality in the nonlinear optical second-harmonic generation (SHG). By physically reversing the beam path, we show that the measured SHG intensity can change by at least a factor of six between forward and backward propagation over a wide bandwidth exceeding $250\,\mathrm{meV}$. Supported by density-functional theory calculations, we establish the linearly dispersive bands emerging from Weyl nodes as the origin of the extreme bandwidth. Intriguingly, the NODE directionality is directly controlled by the direc-

tion of magnetization. By utilizing the electronically conductive semimetallic nature of CeAlSi, we demonstrate current-induced magnetization switching and thus electrical control of the NODE in a mesoscopic spintronic device structure with current densities as small as $5\,\mathrm{kA/cm^2}$. Our results advance ongoing research to identify novel nonlinear optical/transport phenomena in magnetic topological materials. The NODE also provides a way to measure the phase of nonlinear optical susceptibilities and further opens new pathways for the unidirectional manipulation of light such as electrically controlled optical isolators.

MAIN

Diode effects, i.e., phenomena that exhibit a preferred direction, are at the heart of new fundamental physics and modern technologies. A primary example is an electrical diode, which readily conducts current in one direction, but has a high resistance in the opposite direction. In analogy to electrical diodes, optical diodes are characterized by a directionally asymmetric propagation of light. Recent theoretical studies have shown that such an optical diode effect can reveal fundamentally new physics, such as the quantum metric of Bloch wavefunctions[1–3]. Moreover, the optical diode would be a crucial component of various optical technologies including the photonics, where light instead of electrical current is envisioned as information carrier. For instance, in the microwave regime, the optical diode effect has been proposed for telecommunications[4,5]. Such prospects have inspired a flurry of experimental studies of the optical diode effect (also known as the nonreciprocal directional dichroism) especially in magnetoelectric wide-bandgap insulators[6,7]. However, the observed optical diode effect is typically very weak with the difference between forward and backward propagation being less than 1% unless the photon energy is tuned to specific narrow electronic or magnetic resonances with bandwidths often below 5 meV.

In addition to its propagation direction, light has another important degree of freedom, the color (frequency). Therefore, it is possible to conceptualize the nonlinear optical diode effect, where the photon frequency changes during the diode process. A second-order diode effect is a process where the optical second-harmonic generation (SHG) of a material along the forward and backward propagation directions differ. In terms of fundamental physics, the nonlinear optical diode effect (NODE) may reveal novel quantum geometrical phenomena distinct from the linear optical diode[8–11]. Also, nonlinear optical processes (e.g. SHG) can lead to a much stronger diode effect (i.e., a larger contrast between the forward and backward direction) as SHG supports much stronger crystallographic selection rules[12,13]. In terms of technology, the NODE may also enable novel optical applications such as unidirectional and mode-locked lasers[14] and novel designs for optical isolators for optical communication[15].

Recently, Weyl semimetals have emerged as an attractive system to explore various novel electrical and optical

phenomena, due to its combination of nontrivial quantum geometry and strong symmetry breaking (to generate Weyl fermions, the system has to break space-inversion, or time-reversal, or both). In the electrical regime, a giant electrical diode effect (the nonreciprocal transport) has been observed in Weyl systems[16]. In the optical regime, novel optical diode effect has been theoretically considered[1,2,17] but never probed experimentally. In contrast to conventional magnetoelectric insulators[12,13] (Fig. 1a), the Weyl semimetals host linearly dispersive Weyl cones, which can allow for a wide range of photon energies to excite interband optical transitions in the material (Fig. 1b).

In this paper, we report the observation and manipulation of a giant, broadband NODE in the magnetic Weyl semimetal CeAlSi. We demonstrate that at least a sixfold change in SHG intensity is achievable between forward and backward propagating light over a broad spectral range covering 250 meV. Supported by first-principles calculations, we establish a link between the broadband characteristics and the linearly dispersive Weyl fermions in CeAlSi. We show that the directionality of the NODE is directly related to the magnetic order in CeAlSi. We can switch the magnetic order by passing a current and thus demonstrate electrical control of the NODE. We reveal that this basic opto-spintronic functionality persists in technologically relevant, micromachined device structures with the additional advantage of drastically reduced switching currents.

OBSERVATION OF THE NONLINEAR OPTICAL DIODE EFFECT (NODE) IN CEALSI

CeAlSi belongs to the family of Weyl semimetals with chemical formula $R\mathrm{Al}X$ (R = La-Nd and X=Si or Ge) that recently gained considerable attention as magnetic Weyl semimetals[18–29]. This family is closely related to TaAs[30,31], as they have the same noncentrosymmetric, tetragonal crystal structure (point group $4mm$) and the same valence condition ($R^{3+}[\mathrm{Al}X]^{3-}$ *vs* $\mathrm{Ta}^{3+}\mathrm{As}^{3-}$). The introduction of magnetic rare earth elements (Ce, Pr, or Nd) in $R\mathrm{Al}X$ compounds leads to long-range magnetic order. Depending on the rare earth element, a variety of magnetic structures ranging from simple collinear ferromagnetism to noncollinear magnetism and complex multi-k helical spin structures has been found[19–25]. The interplay between Weyl fermions, inversion symmetry-breaking, and magnetism provides a fertile ground to discover novel emergent quantum electromagnetism in this class of Weyl semimetals.

CeAlSi exhibits a canted ferromagnetic order below $T_\mathrm{C} \sim 8.4\,\mathrm{K}$ (Fig. 1c). The net magnetization points along one of the four symmetry-equivalent in-plane crystallographic directions, $\pm[110]$ and $\pm[\bar{1}10]$ (We define $[110] = +\hat{\mathbf{x}}$, $[\bar{1}10] = +\hat{\mathbf{y}}$, and $[001] = +\hat{\mathbf{z}}$, Fig. 1c). Hence, there are four distinct ferromagnetic states, denoted as $\mathbf{M}_{+\mathrm{x}}$, $\mathbf{M}_{-\mathrm{x}}$, $\mathbf{M}_{+\mathrm{y}}$, and $\mathbf{M}_{-\mathrm{y}}$. Such a $\mathcal{T}$-breaking magnetic ordering on a $\mathcal{P}$-breaking crystal structure makes CeAlSi a promising candidate for the observation of the NODE.

We consider the NODE explicitly by experimentally reversing the light path. As CeAlSi is semimetallic and therefore highly reflective, we consider the NODE here in a reflection geometry (Fig. 1d). We study in particular SHG

from the (001) facet of a CeAlSi single crystal. Therefore, all four magnetic states of CeAlSi exhibit an in-plane net magnetization. We orient the crystal such that the s-polarization of light is parallel to the net magnetization of two out of the four possible magnetic states. We denote those states as $\mathbf{M}_{\pm \mathrm{y}}$ states and the states with net magnetization perpendicular to the s-polarization $\mathbf{M}_{\pm \mathrm{x}}$ states (see coordinate system in Fig. 1d).

In Fig. 1e, we directly compare the spectra for the recorded SHG intensity for the forward propagation direction ($I^{\rightarrow}(2\omega)$) and the backward propagation direction ($I^{\leftarrow}(2\omega)$) for the magnetic $\mathbf{M}_{+\mathrm{y}}$ state. The SHG intensity $I^{\rightarrow}(2\omega)$ in forward direction is more than twice as large as the intensity $I^{\leftarrow}(2\omega)$ in backward direction over the entire considered spectral range of the incident light from 650 meV to 900 meV. Reversing the magnetization reverses the situation (Extended Data Fig. 1a). We thus find that the SHG response exhibits a NODE over a wide range of fundamental photon energies spanning at least 250 meV.

In Figs. 2a,b we show the polarization dependence of $I^{\rightarrow}_{+\mathrm{y}}$ and $I^{\leftarrow}_{+\mathrm{y}}$, respectively, at a fundamental photon energy of 715 meV for the magnetic $\mathbf{M}_{+\mathrm{y}}$ state of CeAlSi. The polarization dependence also clearly reveals the NODE in the SHG response. To further corroborate the nonreciprocal character of the observed SHG, we define the integrated SHG intensity $\langle I \rangle$ as the intensity measured without polarization analysis, thus simultaneously detecting s- and p-polarized SHG light, and averaging over all polarizations of the incident fundamental light. Comparing the integrated SHG intensity between the forward and backward direction gives us a measure of the diode effect independent of the light polarization (i.e., the diode effect for unpolarized light). Interestingly, we find for the magnetic $\mathbf{M}_{+\mathrm{y}}$ state that the integrated SHG intensity $\langle I^{\rightarrow}_{+y} \rangle$ in the forward direction is significantly higher than $\langle I^{\leftarrow}_{+y} \rangle$ in the reversed direction (Fig. 2c). This shows that the NODE is not restricted to particular polarization configurations but a net diode effect can persist even in the case of unpolarized incident light.

MAGNETIC CONTROL OF THE NODE

Interestingly, the directionality of the NODE can be controlled by the magnetic order. In Figs. 2a-c and 2d-e, we compare the results for the $\mathbf{M}_{+\mathrm{y}}$ and $\mathbf{M}_{-\mathrm{y}}$ states, from which we see that the directionality of the NODE is flipped as we flip the magnetization. Thus, while the broken $\mathcal{P}$ symmetry in general activates the NODE, the broken $\mathcal{T}$ symmetry enables controlling its directionality. By selecting either the $\mathbf{M}_{+\mathrm{y}}$ or $\mathbf{M}_{-\mathrm{y}}$ state, we can deterministically set the propagation direction that generates higher integrated SHG intensity.

We can understand the NODE and its magnetic control by the interference of independent SHG tensor components with different origins. In our case, we can use χ_{xxx} and χ_{xxz}. χ_{xxz} arises from the noncentrosymmetric polar lattice of CeAlSi; χ_{xxx} arises from the magnetic order. As shown in Extended Data Fig. 4, the total SHG intensity is given by $|\chi_{xxx}E_x^2 + \chi_{xxz}E_xE_z|^2$. Considering p-polarized incident light, the electric field $\mathbf{E}$ of the light wave is parallel to

$\mathbf{k} \times \hat{\mathbf{y}}$ leading to a $\mathbf{k}$ dependence of the SHG response. Specifically, as we reverse the light propagation direction, we reverse the relative sign between E_x and E_z. Hence, we find $I^{\rightarrow}_{+\mathrm{y}}(2\omega) \propto |\chi_{xxx} + \chi_{xxz}|^2$ and $I^{\leftarrow}_{+\mathrm{y}}(2\omega) \propto |\chi_{xxx} - \chi_{xxz}|^2$. Thus, the NODE is based on a directionally dependent mixing between tensor components. It is interesting to note that the origin of the symmetry breaking that enables those tensor components is not crucial. This is in contrast to the established SHG interference imaging technique which strictly relies on interference between order-parameter dependent and order-parameter independent χ tensor components[32]. As a consequence, a NODE can in principle exist even in non-magnetic materials. Here, however, we explicitly utilize the different origin of χ_{xxx} and χ_{xxz} to control the directionality of the NODE. As we reverse the magnetization direction, we reverse the sign of the magnetic SHG tensor χ_{xxx} but the crystalline SHG tensor component χ_{xxz} remains unchanged. Thus, we find $I^{\rightarrow}_{-\mathrm{y}}(2\omega) \propto |-\chi_{xxx} + \chi_{xxz}|^2$ and $I^{\leftarrow}_{-\mathrm{y}}(2\omega) \propto |-\chi_{xxx} - \chi_{xxz}|^2$, which explains why the NODE directionality flips as we flip the magnetization direction.

ELECTRICAL CONTROL OF THE NODE

The noncentrosymmetric symmetry of CeAlSi supports a magnetoelectric coupling between the magnetization $\mathbf{M}$ and a current $\mathbf{J}$. Microscopically, such a coupling may be either intrinsic[33,34], mediated by strain[35], or relying on the spin-Hall effect[36] and assisted by the Oersted field of the current[37,38]. In all cases, the magnetoelectric coupling is such that a current in the xy-plane favors a magnetization perpendicular to the current in the xy-plane with a fixed handedness as depicted in Fig. 3b, providing a way to control the magnetic domain configuration through an electrical current.

We supply a current in the xy-plane through a pattern of gold electrodes on a (001) facet of the sample as illustrated in Fig. 3b. We can then use SHG to optically detect the magnetization state. Specifically, we choose s-polarized incident light at 715 meV and detect p-polarized SHG, where $\mathbf{M}_{\pm\mathrm{y}}$ states correspond to high and low SHG intensity, respectively (Fig. 2a,b. See also Extended Data Fig. 5 for more systematic characterizations).

Remarkably, we find that passing a current in CeAlSi can directly choose its magnetization direction. Moreover, the selected magnetization persists when the current is removed (i.e., the control is nonvolatile). Specifically, as shown in Fig. 3c, if we pass a negative current of -100 mA along the x-direction and then remove this current, we control the magnetization to be along $+y$ ($\mathbf{M}_{+\mathrm{y}}$); if we pass a positive current of 100 mA and then remove this current, we control the magnetization to be along $-y$ ($\mathbf{M}_{-\mathrm{y}}$). Therefore, the data in Fig. 3c shows that the magnetization of CeAlSi can be controlled by current. Moreover, Fig. 3d shows the results over the course of > 10 consecutive current cycles along opposite directions. We found that the control is highly deterministic, i.e., $-x$ current selects $+y$ magnetization whereas $+x$ current selects $-y$ magnetization. The control is also clearly nonvolatile, i.e., the selected

magnetization persists when the current is reduced to zero. By electrically controlling the NODE, we realize here a basic nonreciprocal nonlinear opto-spintronic functionality.

We note that the above results are obtained on a large mm-sized single crystal. So although the total current needed for the magnetic control appears large (100 mA), the current density is very small. However, as the contacts are deposited on the top surface (Fig. 3b), the spatial distribution of current flow is likely to be inhomogeneous for such a thick bulk crystal (especially along the z direction), so it is hard to reliably estimate the current density. In order to reliably estimate the current density, it is highly desirable to fabricate a miniaturized device. Such a micro-device also helps us to explore the tantalizing potential of electrically controlling the nonlinear optical response of CeAlSi for spintronic applications.

In Fig. 3f, we use focused ion-beam (FIB) milling to fabricate such a micro-device of CeAlSi. The core part of the structure is a free-standing slab of CeAlSi of 126 µm × 29 µm × 2 µm. In order to counter-act the significant magnetic shape anisotropy due to the large aspect ratio and keep the device switchable, we prepared the slab with the long axis along the magnetic hard axis, i.e. at an angle of 45° relative to the x and y directions. The device can be poled into a magnetic single domain state with magnetic fields of about 30 mT. Analogously to the previous bulk measurements, the four magnetic states can be distinguished by their SHG polarization dependence (Extended Data Fig. 7).

Most strikingly, in the absence of external magnetic fields, we can electrically control the magnetic state of the micro-device with dramatically reduced currents. As shown in Fig. 3g, we find that we can change the magnetic state in the FIB device with currents as small as 3 mA corresponding to current densities of around 5 kA/cm^2 in the slab (in this case, we do not see remanent switching possibly due to shape anisotropy and residual strain in the sample[35,39,40]). The magnetic switching is clearly evidenced by a change of the SHG polarization dependence indicative of switching between the $\mathbf{M}_{-\mathrm{x}}$ state at −3 mA and a $\mathbf{M}_{+\mathrm{x}}$ state at 3 mA. Such a reversible electrical control of a magnetic state may be highly desirable for novel device concepts.

OBSERVATION OF A BROADBAND NODE

Note that so far we observed a pronounced NODE for a specific SHG component at 715 meV without deliberate optimization with respect to polarization or photon energy. However, a comparison of Figs. 2a and b reveals that changing the magnetization induces large changes of SHG intensity for certain polarization components and vanishing changes for others. To quantify the NODE, we define the nonreciprocal contrast η as

$$\eta = \frac{I_{+y}^{\rightarrow} - I_{+y}^{\leftarrow}}{I_{+y}^{\rightarrow} + I_{+y}^{\leftarrow}}. \tag{1}$$

The nonreciprocal contrast $\eta = 0$ corresponds to absence of the NODE (i.e., the SHG intensity along forward and backward directions is equal); the nonreciprocal contrast $\eta = \pm 1$ corresponds to extreme NODE (i.e., SHG can only occur along one direction)

In Fig. 4a, we show the evolution of $|\eta|$ for p-polarized SHG as a function of both incoming laser polarization and SHG photon energy. Here, we compare $I^{\rightarrow}_{+y}$ and $I^{\rightarrow}_{-y}$, which is equivalent to comparing $I^{\rightarrow}_{+y}$ and $I^{\leftarrow}_{+y}$ but experimentally more straightforwardly accessible (see Extended Data Fig. 6 for other assessments of η). The figure is characterized by a rich behavior that is mirror symmetric along the 0 and 90 deg directions due to mirror symmetries in CeAlSi. At 715 meV we find that η exhibits maxima at 0 deg/180 deg (p-polarized light) as well as near 90 deg (s-polarized light) but vanishes near 45/135 deg, in agreement with Fig. 2a and b. In Fig. 4b, we show the maximum achievable contrast for each SHG photon energy. The nonreciprocal contrast peaks around 750 meV at 97.2 % corresponding to a more than 70-fold change in SHG intensity. Moreover, we find that a nonreciprocal contrast of at least 73 % (corresponding to a more than 6-fold change) is achievable for all photon energies in the considered spectral range between 650 meV and 900 meV.

BROADBAND NODE FROM FIRST PRINCIPLES

In order to understand the microscopic origin of the NODE, we directly compute the NODE from the electronic structure of CeAlSi. Specifically, the NODE is the difference in SHG intensity between opposite propagation directions, which is determined by the two momentum-space resolved quantities $\kappa^{\rightarrow}$ and $\kappa^{\leftarrow}$ as (see methods, Eq. (8)):

$$\text{NODE} = I^{\rightarrow} - I^{\leftarrow} = |\int_{BZ} \kappa^{\rightarrow}\, d^3\mathbf{k}|^2 - |\int_{BZ} \kappa^{\leftarrow}\, d^3\mathbf{k}|^2. \tag{2}$$

Here, $\kappa^{\rightarrow(\leftarrow)} = \xi_{ijk} E_j^{\rightarrow(\leftarrow)} E_k^{\rightarrow(\leftarrow)} A_k^{\rightarrow(\leftarrow)}$, where $\mathbf{E}^{\rightarrow(\leftarrow)}$ is the electric field of the incident light for the forward and backward propagation direction, $\mathbf{A}^{\rightarrow(\leftarrow)}$ is a projector to select either the s or p polarized SHG response, and ξ_{ijk} is the k-space resolved contribution to the nonlinear optical susceptibility (ξ_{ijk} is directly computed from the band structure of CeAlSi, see methods Eqs. (5) and (6)).

Figure 4c shows a section of the band structure of CeAlSi consistent with previous first-principles calculations[22] (see methods for further details). Along with the band structure, we show in Fig. 4d the magnitude of $\kappa^{\rightarrow}$ and $\kappa^{\leftarrow}$ in the band structure of CeAlSi (for $\hbar\omega = 750$ meV). We see from Fig. 4d that discrete $\mathbf{k}$ points contribute significantly. By comparing Figs. 4c and d, it is clear that these are the states which allow for optical transitions at ω or 2ω across the Fermi energy. Importantly, the magnitude of $\kappa^{\rightarrow}$ and $\kappa^{\leftarrow}$ differs significantly, giving rise to the observed NODE.

To understand the band structure origin of the broadband nature of the NODE in CeAlSi, we vary the incident

photon energy from 650 meV to 850 meV. We can observe two qualitatively different behaviors (Fig. 4e). On the one hand, we notice a few contributions such as near the Γ point along the $\Gamma - \Sigma$ line that occur only at specific photon energies (here 650 meV). The bands at that **k** point are relatively flat. As the photon energy changes, such contributions disappear, which is indicative of a typical electronic resonance. Despite the apparent size of this resonant contribution, the spectrum of all SHG tensor components evolves smoothly towards 650 meV indicating an overall negligible effect (Ext. Data Fig. 8). On the other hand, the majority of the SHG response arises at **k** points where the electronic bands are linearly dispersive. Accordingly, as we vary the incident photon energy, those contributions only shift slightly to different **k** points but remain comparable in magnitude. This observation of SHG originating from linearly dispersive bands is qualitatively different from the conventional resonance picture. Moreover, we thus see that the broadband NODE in CeAlSi ultimately arises from the linearly dispersive bands in the vicinity of the Weyl nodes.

DISCUSSION

In summary, we explored the nonlinear optical response of the magnetic Weyl semimetal CeAlSi using SHG spectroscopy. In addition to the crystallographic (time-reversal symmetric) SHG, we observe magnetic (time-reversal asymmetric) SHG, which represents the first observation of magnetic SHG in a topologically nontrivial material. By physically reversing the light path, we revealed a pronounced NODE. Specifically, we found a sizable nonreciprocal contrast of at least 73% over a remarkable spectral range exceeding 250 meV — two orders of magnitude wider than previous reports.

Microscopically, our DFT calculations show that the extreme broadband NODE is directly related to the electronic band structure. The SHG response emerges from linearly dispersive bands that naturally occur near the Fermi energy in a Weyl semimetal. The linear dispersion allows for strong optical responses over a wide range of frequencies.

Our observations open up a number of intriguing possibilities. First, it suggests the NODE as a powerful method to measure the phase of optical properties. All optical processes (e.g., SHG, Raman) are governed by the corresponding susceptibility tensor, which is determined by the material. Hence, inversely, by measuring the SHG, Raman, or other optical process, we can learn about the symmetry and electronic properties of a material. However, typically we only access the magnitude of the susceptibility, whereas the sign or phase is hard to probe. Here, as we showed above, the NODE arises from the directionally dependent mixing between tensor components which provides insights into their relative phases. It would be interesting to test the optical diode effect for other optical processes such as high-harmonic generation[41], Raman scattering[42], and optically generated spin currents[43], where interesting phenomena hinting nonreciprocity have been observed. Second, we note the low current density associated with the switching of

magnetic order in CeAlSi. It would be of interest to perform future studies to understand its microscopic mechanism and to test it on other magnetic and noncentrosymmetric Weyl fermion systems. The low-current switching in combination with the extreme broadband character of the NODE, may enable fundamentally new device concepts for photonic circuits. From a fundamental point of view, our observation of a broadband NODE is testament to the exotic electromagnetic responses that can be discovered in novel quantum magnets.

* current address: Max-Born Institute for Nonlinear Optics and Short Pulse Spectroscopy, Berlin, Germany. Email: christian.tzschaschel@mbi-berlin.de

† Email: suyangxu@fas.harvard.edu

[1] M. F. Lapa, T. L. Hughes, Semiclassical wave packet dynamics in nonuniform electric fields, *Phys. Rev. B* **99**, 121111 (2019).

[2] Y. Gao, D. Xiao, Nonreciprocal Directional Dichroism Induced by the Quantum Metric Dipole, *Phys. Rev. Lett.* **122**, 227402 (2019).

[3] Y. Zhang, L. Shi, C. T. Chan, K. H. Fung, K. Chang, Geometrical Theory of Electromagnetic Nonreciprocity, *Phys. Rev. Lett.* **130**, 203801 (2023).

[4] A. Sabharwal, *et al.*, In-Band Full-Duplex Wireless: Challenges and Opportunities, *IEEE J. Sel. Areas Commun.* **32**, 1637 (2014).

[5] N. Reiskarimian, H. Krishnaswamy, Magnetic-free non-reciprocity based on staggered commutation, *Nat. Commun.* **7** (2016).

[6] M. Fiebig, Revival of the magnetoelectric effect, *J. Phys. D: Appl. Phys.* **38**, R123 (2005).

[7] N. A. Spaldin, R. Ramesh, Advances in magnetoelectric multiferroics, *Nat. Mater.* **18**, 203 (2019).

[8] N. Nagaosa, T. Morimoto, Y. Tokura, Transport, magnetic and optical properties of Weyl materials, *Nat. Rev. Mater.* **5**, 621 (2020).

[9] J. Orenstein, *et al.*, Topology and Symmetry of Quantum Materials via Nonlinear Optical Responses, *Annu. Rev. Condens. Matter Phys* **12**, 247 (2021).

[10] Q. Ma, A. G. Grushin, K. S. Burch, Topology and geometry under the nonlinear electromagnetic spotlight, *Nat. Mater.* **20**, 1601 (2021).

[11] N. Nagaosa, Nonlinear optical responses in noncentrosymmetric quantum materials, *Ann. Phys.* 169146 (2022).

[12] S. Toyoda, M. Fiebig, T. hisa Arima, Y. Tokura, N. Ogawa, Nonreciprocal second harmonic generation in a magnetoelectric material, *Sci. Adv.* **7** (2021).

[13] J. Mund, *et al.*, Toroidal nonreciprocity of optical second harmonic generation, *Phys. Rev. B* **103**, L180410 (2021).

[14] L. Fan, *et al.*, An All-Silicon Passive Optical Diode, *Science* **335**, 447 (2012).

[15] L. Feng, *et al.*, Nonreciprocal Light Propagation in a Silicon Photonic Circuit, *Science* **333**, 729 (2011).

[16] Y. Tokura, N. Nagaosa, Nonreciprocal responses from non-centrosymmetric quantum materials, *Nat. Commun.* **9**, 3740 (2018).

[17] S. Nandy, D. A. Pesin, Nonreciprocal optics and magnetotransport in Weyl metals as signatures of band topology, *Phys. Rev. B* **106**, L041108 (2022).

[18] G. Chang, *et al.*, Magnetic and noncentrosymmetric Weyl fermion semimetals in the RAlGe family of compounds (R = rare earth), *Phys. Rev. B* **97**, 041104 (2018).

[19] H. Hodovanets, *et al.*, Single-crystal investigation of the proposed type-II Weyl semimetal CeAlGe, *Phys. Rev. B* **98**, 245132 (2018).

[20] T. Suzuki, *et al.*, Singular angular magnetoresistance in a magnetic nodal semimetal, *Science* **365**, 377 (2019).

[21] P. Puphal, *et al.*, Topological Magnetic Phase in the Candidate Weyl Semimetal CeAlGe, *Phys. Rev. Lett.* **124**, 017202 (2020).

[22] H.-Y. Yang, *et al.*, Noncollinear ferromagnetic Weyl semimetal with anisotropic anomalous Hall effect, *Phys. Rev. B* **103**, 115143 (2021).

[23] Y. Sun, *et al.*, Mapping domain-wall topology in the magnetic Weyl semimetal CeAlSi, *Phys. Rev. B* **104**, 235119 (2021).

[24] H. Su, *et al.*, Multiple Weyl fermions in the noncentrosymmetric semimetal LaAlSi, *Phys. Rev. B* **103**, 165128 (2021).

[25] J. Gaudet, *et al.*, Weyl-mediated helical magnetism in NdAlSi, *Nat. Mater.* **20**, 1650 (2021).

[26] X. Yao, *et al.*, Large Topological Hall Effect and Spiral Magnetic Order in the Weyl Semimetal SmAlSi, *Phys. Rev. X* **13**, 011035 (2023).

[27] M. S. Alam, *et al.*, Sign change of anomalous Hall effect and anomalous Nernst effect in the Weyl semimetal CeAlSi, *Phys. Rev. B* **107**, 085102 (2023).

[28] Y. Zhang, *et al.*, Kramers nodal lines and Weyl fermions in SmAlSi, *arxiv:2210.13538* (2022).

[29] H. Hodovanets, *et al.*, Anomalous symmetry breaking in the Weyl semimetal CeAlGe, *Phys. Rev. B* **106**, 235102 (2022).

[30] S.-Y. Xu, *et al.*, Discovery of a Weyl fermion semimetal and topological Fermi arcs, *Science* **349**, 613 (2015).

[31] B. Lv, *et al.*, Experimental Discovery of Weyl Semimetal TaAs, *Phys. Rev. X* **5**, 031013 (2015).

[32] M. Fiebig, V. V. Pavlov, R. V. Pisarev, Second-harmonic generation as a tool for studying electronic and magnetic structures of crystals: review, *J. Opt. Soc. Am. B* **22**, 96 (2005).

[33] R. Birss, *Symmetry and Magnetism* (North Holland Publishing Company, 1966), second edn.

[34] A. Johansson, J. Henk, I. Mertig, Edelstein effect in Weyl semimetals, *Phys. Rev. B* **97**, 085417 (2018).

[35] B. Xu, *et al.*, Picoscale Magnetoelasticity Governs Heterogeneous Magnetic Domains in a Noncentrosymmetric Ferromagnetic Weyl Semimetal, *Adv. Quantum Technol.* **4**, 2000101 (2021).

[36] J. Sinova, S. O. Valenzuela, J. Wunderlich, C. Back, T. Jungwirth, Spin Hall effects, *Rev. Mod. Phys.* **87**, 1213 (2015).

[37] S. Krause, L. Berbil-Bautista, G. Herzog, M. Bode, R. Wiesendanger, Current-Induced Magnetization Switching with a Spin-Polarized Scanning Tunneling Microscope, *Science* **317**, 1537 (2007).

[38] J. Mendil, M. Trassin, Q. Bu, M. Fiebig, P. Gambardella, Current-induced switching of YIG/Pt bilayers with in-plane magnetization due to Oersted fields, *Appl. Phys. Lett.* **114**, 172404 (2019).

[39] J. Dubowik, Shape anisotropy of magnetic heterostructures, *Phys. Rev. B* **54**, 1088 (1996).

[40] Z. Wang, *et al.*, Engineered Magnetic Shape Anisotropy in $BiFeO_3$–$CoFe_2O_4$ Self-Assembled Thin Films, *ACS Nano* **7**, 3447 (2013).

[41] C. Heide, *et al.*, Probing topological phase transitions using high-harmonic generation, *Nat. Photonics* **16**, 620 (2022).

[42] Y. Wang, *et al.*, Axial Higgs mode detected by quantum pathway interference in RTe_3, *Nature* **606**, 896 (2022).

[43] J. Li, *et al.*, Spin current from sub-terahertz-generated antiferromagnetic magnons, *Nature* **578**, 70 (2020).

[44] P. Hohenberg, W. Kohn, Inhomogeneous Electron Gas, *Phys. Rev.* **136**, B864 (1964).

[45] G. Kresse, J. Furthmüller, Efficiency of ab-initio total energy calculations for metals and semiconductors using a plane-wave basis set, *Comput. Mater. Sci.* **6**, 15 (1996).

[46] J. P. Perdew, K. Burke, M. Ernzerhof, Generalized Gradient Approximation Made Simple, *Phys. Rev. Lett.* **77**, 3865 (1996).

[47] D. C. Langreth, M. J. Mehl, Beyond the local-density approximation in calculations of ground-state electronic properties, *Phys. Rev. B* **28**, 1809 (1983).

[48] A. A. Mostofi, *et al.*, An updated version of wannier90: A tool for obtaining maximally-localised Wannier functions, *Comput. Phys. Commun.* **185**, 2309 (2014).

[49] D. Gresch, *et al.*, Automated construction of symmetrized Wannier-like tight-binding models from *ab initio* calculations, *Phys. Rev. Materials* **2**, 103805 (2018).

[50] D. E. Parker, T. Morimoto, J. Orenstein, J. E. Moore, Diagrammatic approach to nonlinear optical response with application to Weyl semimetals, *Phys. Rev. B* **99**, 045121 (2019).

[51] K. Takasan, T. Morimoto, J. Orenstein, J. E. Moore, Current-induced second harmonic generation in inversion-symmetric Dirac and Weyl semimetals, *Phys. Rev. B* **104**, l161202 (2021).

[52] T. Morimoto, N. Nagaosa, Topological nature of nonlinear optical effects in solids, *Sci. Adv.* **2**, e1501524 (2016).

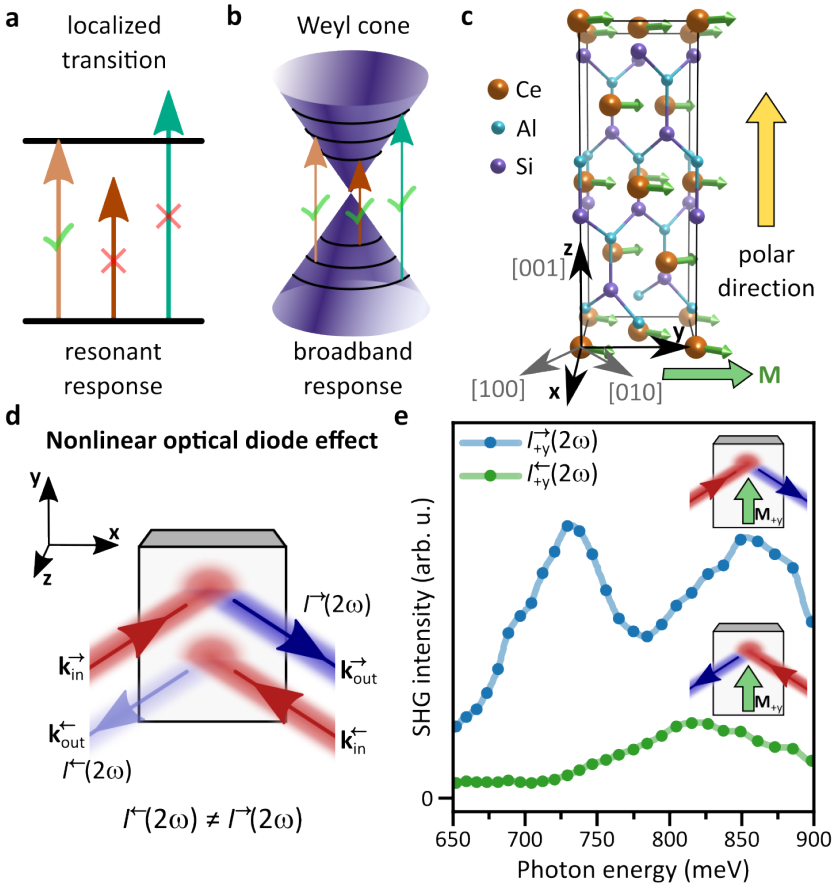

FIG. 1. **Observation of a broadband NODE in the magnetic Weyl semimetal CeAlSi. a,** For a localized electronic transition, such as in wide-gap insulators, only specific photon energies can drive the transition resulting in a resonant response. **b,** For dispersive bands such as Weyl cones, different photon energies can drive transitions leading to a broadband response. **c,** Crystal structure of the magnetic Weyl semimetal CeAlSi. We define $+\hat{\mathbf{x}} = [110]$, $+\hat{\mathbf{y}} = [\bar{1}10]$, and $+\hat{\mathbf{z}} = [001]$ relative to the tetragonal unit cell of (paramagnetic) CeAlSi. **d,** Definition of the NODE in reflection. Reversing the light path by swapping light source and detector corresponds to changing the light $\mathbf{k}$ vectors $\mathbf{k}_{\text{in}}^{\rightarrow}$ and $\mathbf{k}_{\text{out}}^{\rightarrow}$ to $\mathbf{k}_{\text{in}}^{\leftarrow}$ and $\mathbf{k}_{\text{out}}^{\leftarrow}$. A NODE is evidenced by a difference between intensities $I^{\rightarrow}(2\omega)$ in forward direction and $I^{\leftarrow}(2\omega)$ in reversed direction. **e,** Observation of a broadband NODE in the $\mathbf{M}_{+\text{y}}$ state of CeAlSi. $I_{+y}^{\rightarrow}(2\omega) \gg I_{+y}^{\leftarrow}(2\omega)$ over a broad range >250 meV.

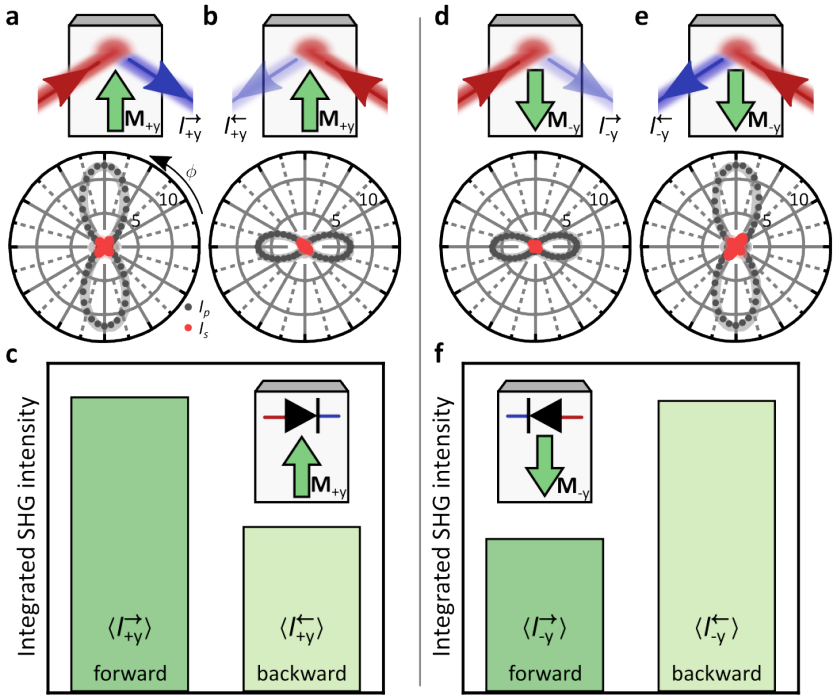

FIG. 2. **Magnetic control of the NODE. a,b,** Polarization-dependent SHG for both propagation directions of the $\mathbf{M}_{+y}$ state (fundamental photon energy 715 meV). **c,** Integrated SHG intensity of the $\mathbf{M}_{+y}$ state for both propagation directions. The integrated SHG intensity is defined as the intensity measured without polarization analysis, thus simultaneously detecting s- and p-polarized SHG light, and averaging over all polarizations of the incident fundamental light. **d-f,** Analogous to panels **a-c** but for the $\mathbf{M}_{-y}$ state. Solid lines are fits with one consistent set of ED-SHG $\mathcal{X}$ tensor components (see methods). The magnetic state of CeAlSi controls the directionality of the NODE enabling a switchable nonlinear optical diode.

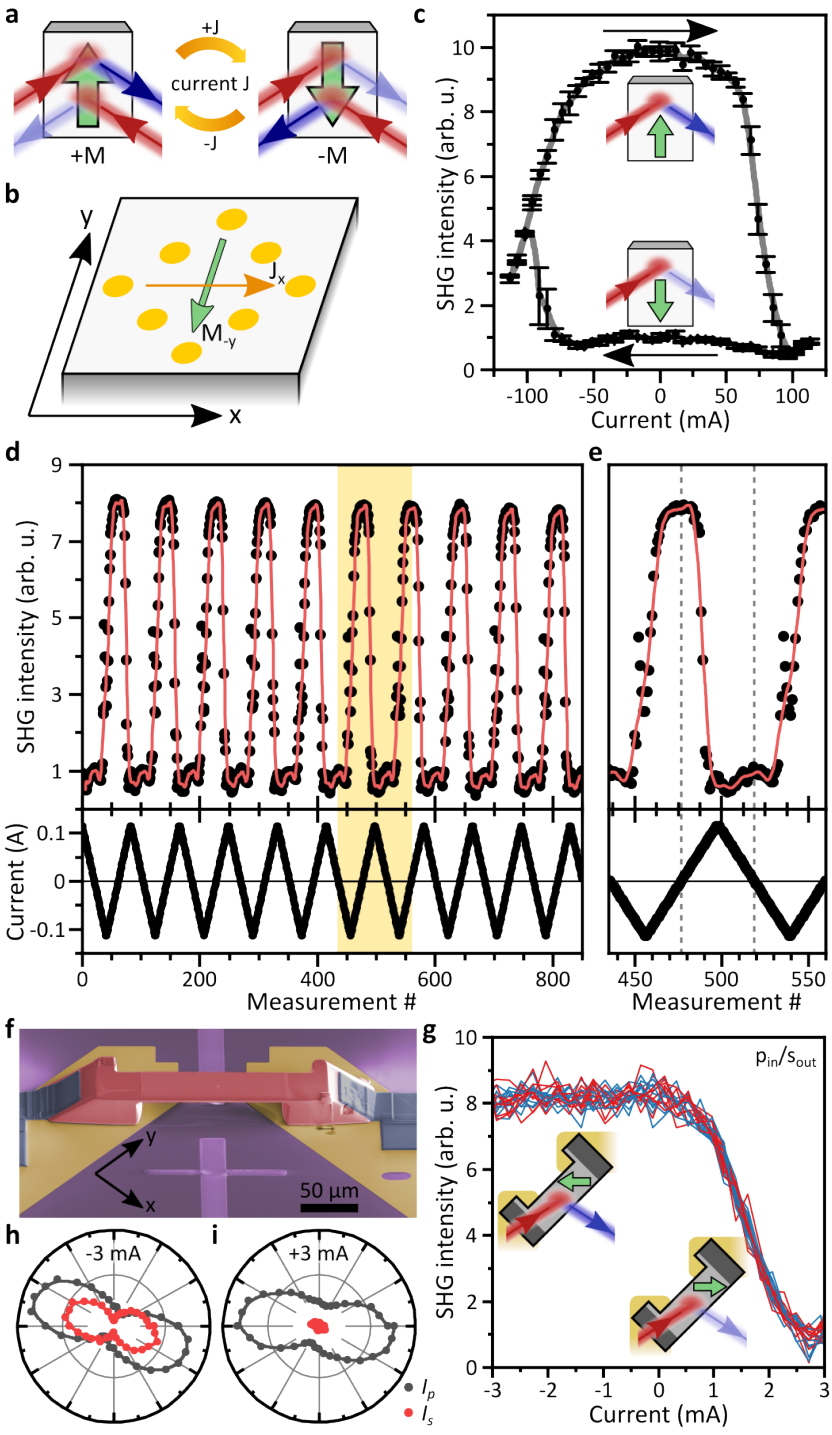

FIG. 3. **Electrical control of the NODE. a,** Schematic of a device concept. Current-induced magnetization switching enables electrical control of the NODE. **b,** We deposit eight gold electrodes on the top surface of a bulk mm-sized CeAlSi crystal, which allows us to pass current through the sample. Here, we focus on current along the $\hat{\mathbf{x}}$ direction, which causes magnetization switching along the $\hat{\mathbf{y}}$ direction. Microscopically, the switching mechanism may be based on a current-induced magnetization[34,36] or an effective magnetic field[35,37,38]. **c,** Current hysteresis loop. A current of 100 mA fully switches the magnetization. We measure p-polarized SHG in forward direction with s-polarized incident light. Therefore, high and low intensity correspond to $\mathbf{M}_{+y}$ and $\mathbf{M}_{-y}$ states, respectively. **d,** Current-induced magnetization switching is highly reproducible. Here, we show 10 consecutive cycles. **e,** Enlarged view of the highlighted region in d. Dashed lines correspond to the remanent states. **f,** Scanning electron microscopy image of a micro-sized device manufactured by focused ion beam milling of CeAlSi (red) on gold electrodes (gold). Platinum contacts (gray) ensure good electrical connections. **g,** Currents as small as 3 mA can control the magnetization state. Red and blue curves correspond to consecutive measurements with increasing and decreasing current, respectively. We detect s-polarized SHG, which can discriminate $\mathbf{M}_{\pm x}$ states. A hysteresis is suppressed possibly due to shape anisotropy or residual strain in the sample[35,39,40]. **h,i,** SHG polarization dependence under application of −3 mA and +3 mA, respectively. Changes are most prominent for s-polarized SHG (red).

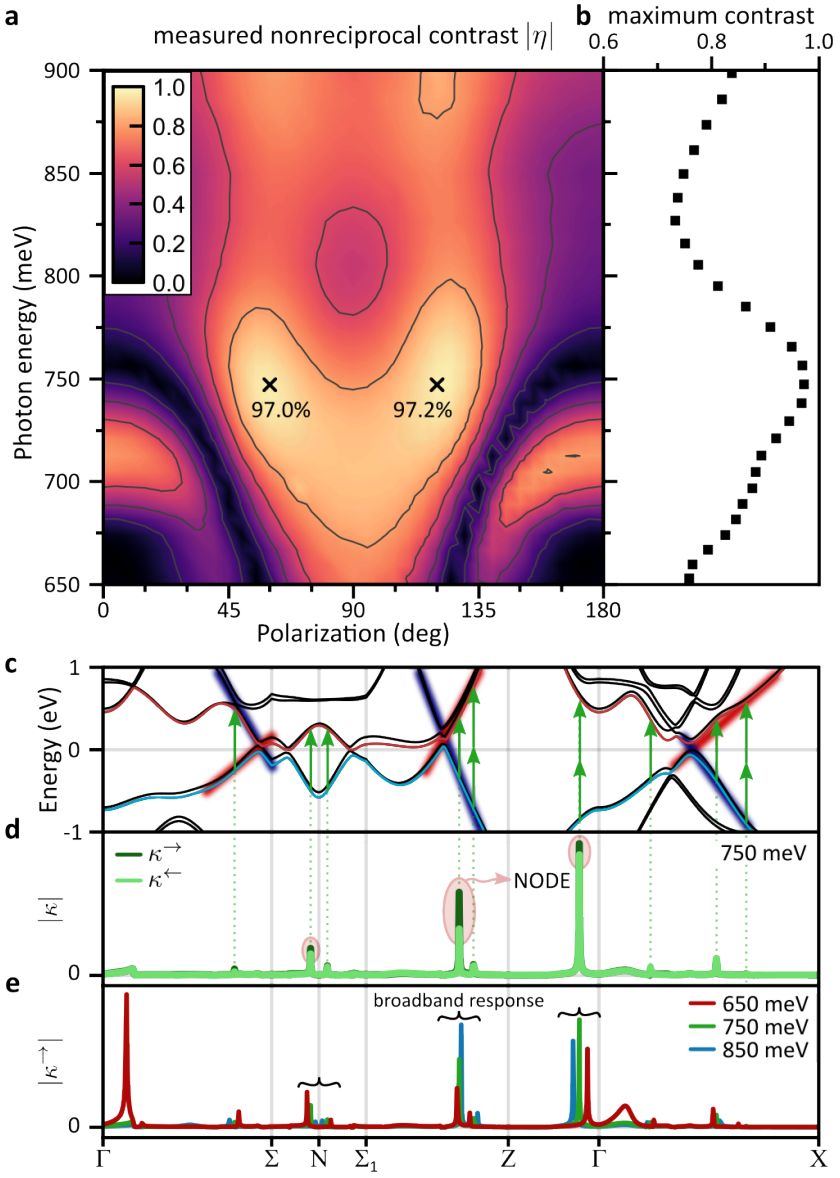

FIG. 4. **NODE spectroscopy and its microscopic origin from the linearly dispersive bands. a,** Measured absolute value of the nonreciprocal contrast $|\eta|$ between $\mathbf{M}_{\pm y}$ states for p-polarized SHG in forward direction as a function of incident photon energy and polarization. **b,** Maximum achievable nonreciprocal contrast by varying incident polarization as function of photon energy. A contrast of at least 73% corresponding to a six-fold change in SHG intensity is achievable over the whole considered spectral range. **c,** Band structure of CeAlSi calculated from first principles in the $\mathbf{M}_{+y}$ state. **d,** Momentum-space resolved contributions $\kappa^{\rightarrow}$ and $\kappa^{\leftarrow}$ at 750 meV for forward and backward propagating beams. The difference between $\kappa^{\rightarrow}$ and $\kappa^{\leftarrow}$ leads to the NODE (see text). For clarity, we only show here contributions arising from the valence band marked in blue and the conduction band marked in red. **e,** Momentum-space resolved contributions to the SHG intensity in forward direction at incident photon energies $\hbar\omega$ of 650 meV, 750 meV, and 850 meV. Most contributions arise at **k** points where electronic bands are linearly dispersive thus giving rise to a broadband response.

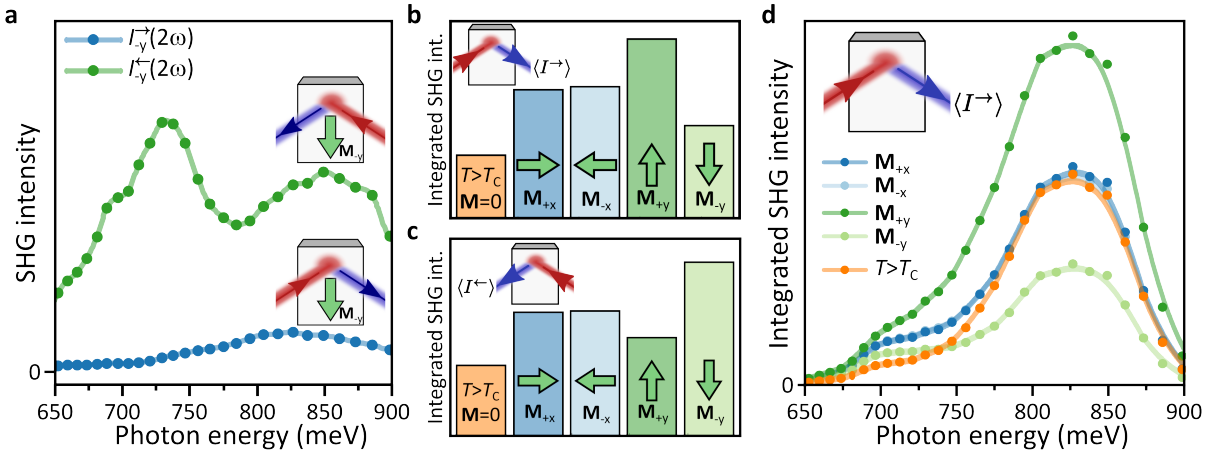

Extendend Data Fig. 1. **Further observations of the NODE. a,** Observation of a broadband NODE in the $\mathbf{M}_{-\mathrm{y}}$ state. $I^{\rightarrow}_{-y}(2\omega) \ll I^{\leftarrow}_{-y}(2\omega)$ over a broad range >250 meV. **b,** Integrated SHG in forward direction at 715 meV. **c,** Integrated SHG in backward direction at 715 meV. In contrast to the forward direction, $\langle I^{\leftarrow}_{+y}\rangle < \langle I^{\leftarrow}_{-y}\rangle$. The integrated SHG intensity in the $\mathbf{M}_{\pm \mathrm{x}}$ states is always identical for the two propagation directions. **d,** Spectra of the integrated SHG intensity $\langle I^{\rightarrow}\rangle$ in forward direction for all magnetic states and in the paramagnetic phase. $\langle I^{\rightarrow}_{+x}\rangle = \langle I^{\rightarrow}_{-x}\rangle$ due to m_y mirror operation (Ext. Data. Fig. 3).

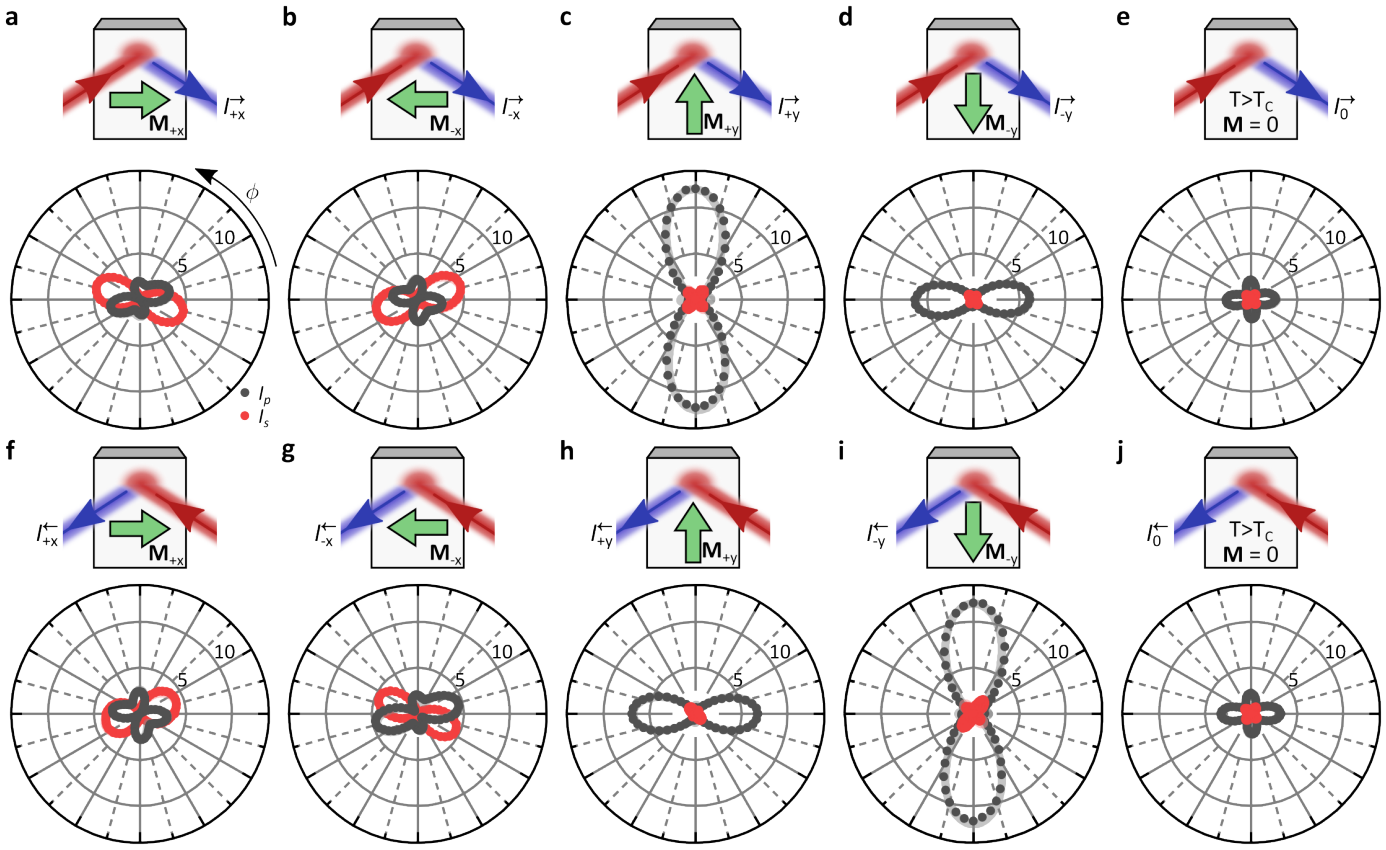

Extendend Data Fig. 2. **SHG Polarization dependencies. a-e,** in forward direction and **f-j,** in backward direction. $I^{\mathbf{k}}_{\mathbf{M}}(\phi) = I^{-\mathbf{k}}_{-\mathbf{M}}(\phi)$ always holds (see Ext. Data Fig. 3 for details). Moreover, reversing the light propagation direction is equivalent to reversing the magnetization. Only the SHG above T_C is reciprocal. All measurements were taken at $\hbar\omega = 715\,\mathrm{meV}$.

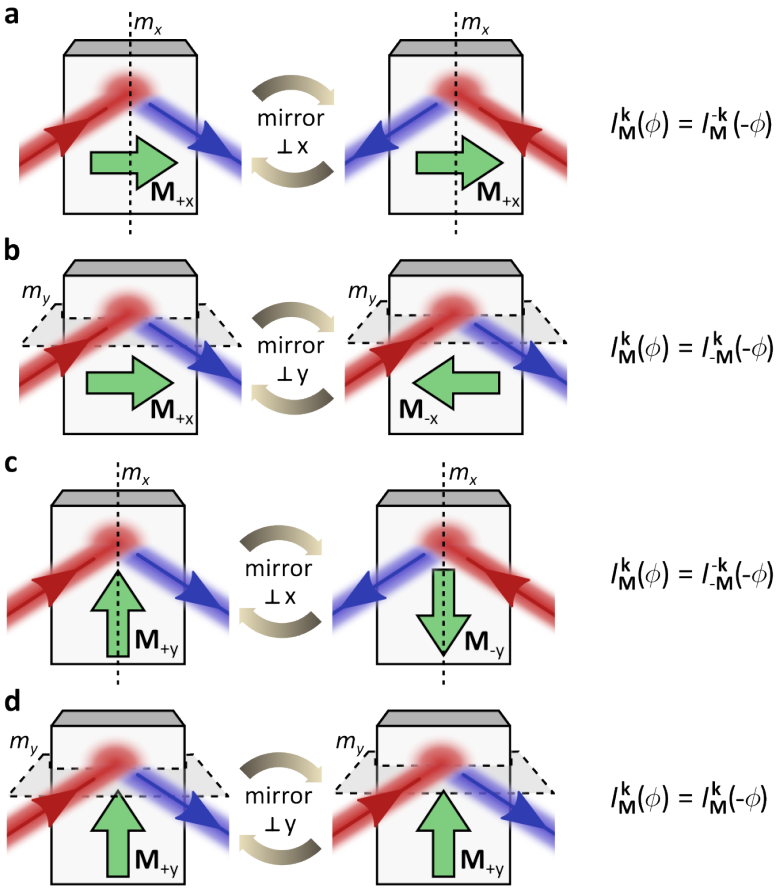

Extendend Data Fig. 3. **Consequences of mirror symmetries in CeAlSi.** Mirror symmetries of the paramagnetic crystal lattice restore certain symmetries in the SHG polarization dependencies (Fig. 2 and Ext. Data Fig. 2). To see this, we consider the effect of the mirror operations m_x and m_y on the magnetization, propagation direction, and light polarization. In general, the mirror operation m_x reverses the propagation direction ($\mathbf{k} \rightarrow -\mathbf{k}$) (a,c) while the mirror operation m_y preserves $\mathbf{k}$ (b,d). Both mirror operations individually transform the linear light polarization from an angle ϕ to $-\phi$ relative to p-polarized light. **a,** In the $\mathbf{M}_{\pm x}$ states, m_x preserves the magnetization along $\hat{\mathbf{x}}$ ($\mathbf{M}_{\pm x} \rightarrow \mathbf{M}_{\pm x}$). Therefore, the SHG intensity $I^{\mathbf{k}}_{\mathbf{M}}(\phi)$ has the symmetry $I^{\mathbf{k}}_{\mathbf{M}}(\phi) = I^{-\mathbf{k}}_{\mathbf{M}}(-\phi)$ (Ext. Data Figs. 2(a,b) are mirror symmetric to Ext. Data Figs. 2(f,g)). **b,** m_y reverses the magnetization along $\hat{\mathbf{x}}$ ($\mathbf{M}_{\pm x} \rightarrow \mathbf{M}_{\mp x}$). Thus, $I^{\mathbf{k}}_{\mathbf{M}}(\phi) = I^{\mathbf{k}}_{-\mathbf{M}}(-\phi)$ (Ext. Data Figs. 2(a,f) are mirror symmetric to Ext. Data Figs. 2(b,g)). **c,** In the $\mathbf{M}_{\pm y}$ states, m_x reverses the magnetization along $\hat{\mathbf{y}}$ ($\mathbf{M}_{\pm y} \rightarrow \mathbf{M}_{\mp y}$).Thus, $I^{\mathbf{k}}_{\mathbf{M}}(\phi) = I^{-\mathbf{k}}_{-\mathbf{M}}(-\phi)$ (Ext. Data Figs. 2(c,d) are symmetric to of Ext. Data Figs. 2(i,h)). **d,** m_y preserves the magnetization along $\hat{\mathbf{y}}$ ($\mathbf{M}_{\pm y} \rightarrow \mathbf{M}_{\pm y}$). Thus, $I^{\mathbf{k}}_{\mathbf{M}}(\phi) = I^{\mathbf{k}}_{\mathbf{M}}(-\phi)$ (Ext. Data Figs. 2(c,d,h,i) are individually mirror symmetric). The application of both mirror operations in any magnetic state enforces $I^{\mathbf{k}}_{\mathbf{M}}(\phi) = I^{-\mathbf{k}}_{-\mathbf{M}}(\phi)$. Thus, reversing both the magnetization and the propagation direction always preserves the SHG polarization dependence.

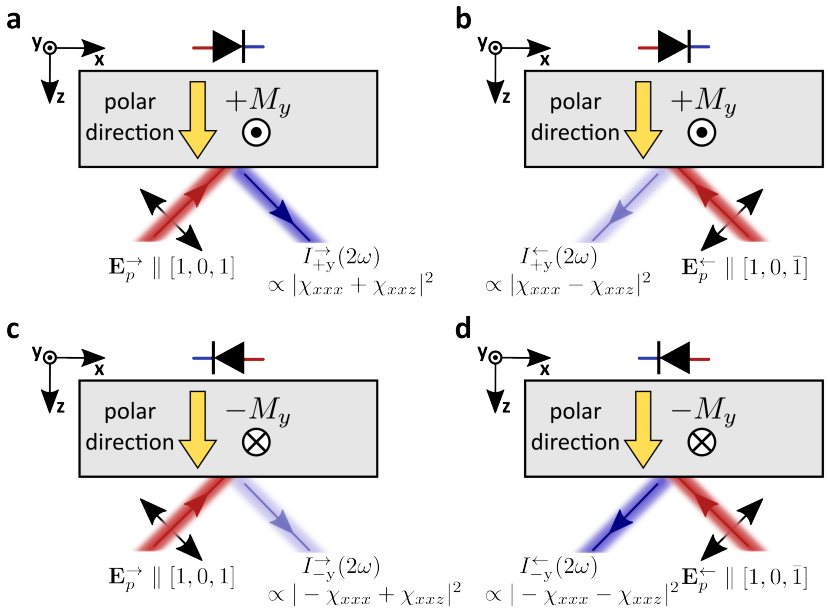

Extendend Data Fig. 4. **Minimal example for the observation and manipulation of the NODE.** We consider a fictitious noncentrosymmetric material for which χ_{xxx} and χ_{xxz} are the only nonvanishing SHG tensor components in an orientation analogous to Fig. 1d. For p-polarized light, the electric field $\mathbf{E}_p(\omega)$ is in general parallel to $\mathbf{k} \times \hat{\mathbf{y}}$. The detected SHG intensity is proportional to the induced nonlinear polarization $I(2\omega) \propto |\sum_i P_i(2\omega)|^2 \propto |\sum_{i,j,k} \chi_{ijk} E_j(\omega) E_k(\omega)|^2 = |\chi_{xxx} E_{p,x}^2 + \chi_{xxz} E_{p,x} E_{p,z}|^2$. Specifically for an angle of incidence of 45°, the electric field is parallel to **a,** $[1,0,1]$ in forward direction and **b,** parallel to $[1,0,\bar{1}]$ in backward direction. Thus, $I^{\rightarrow}(2\omega) \propto |\chi_{xxx} + \chi_{xxz}|^2$ and $I^{\leftarrow}(2\omega) \propto |\chi_{xxx} - \chi_{xxz}|^2 \neq I^{\rightarrow}(2\omega)|^2$. We therefore observe a NODE in this minimal example. **c,d,** Assuming that the χ_{xxz} arises from a polar crystal structure whereas χ_{xxx} is due to magnetic order (as in the case of CeAlSi), allows the manipulation of the NODE as switching the magnetization reverses the directionality.

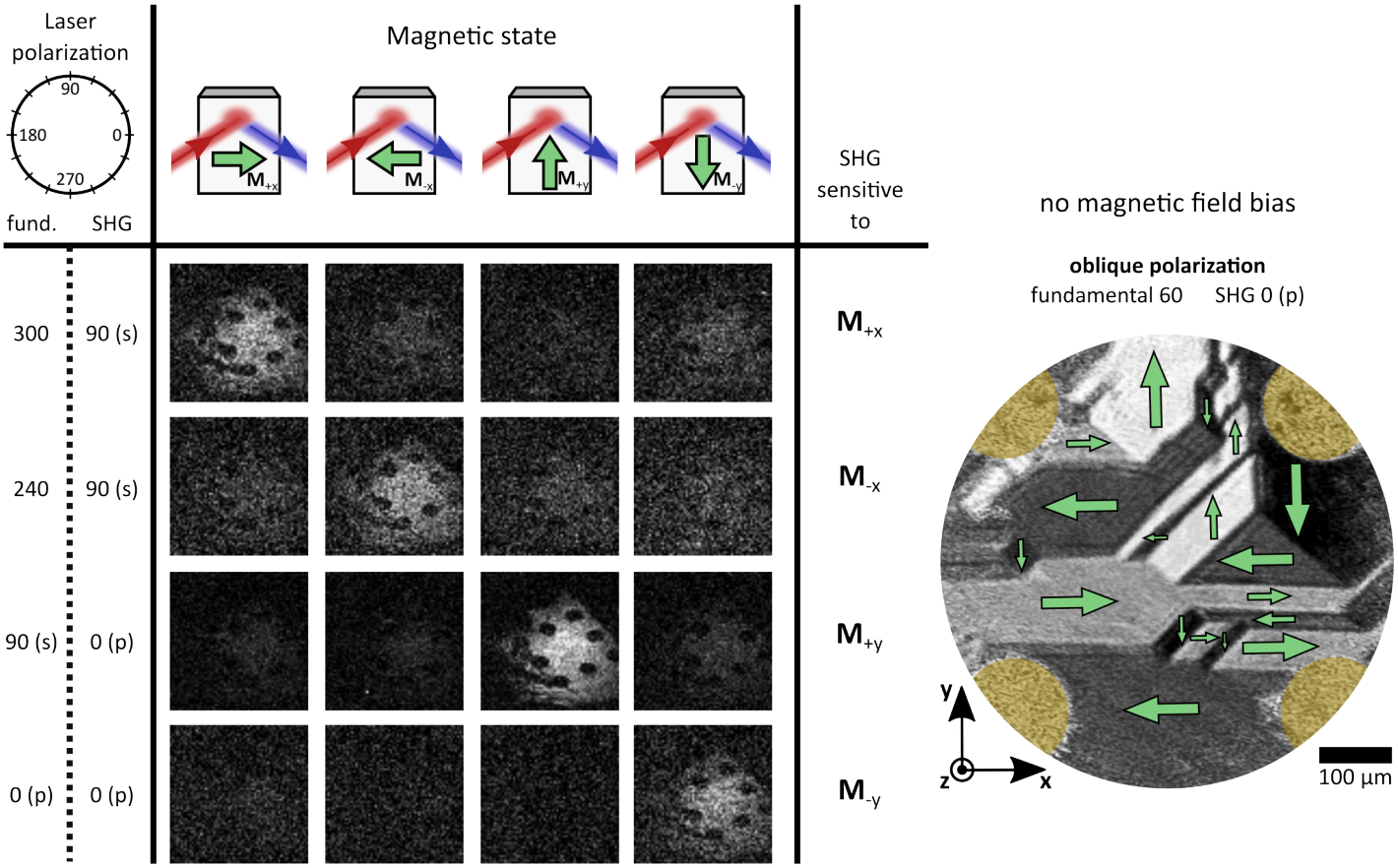

Extendend Data Fig. 5. **Domain assignment.** The unique polarization dependence of the SHG in all four magnetic states (Ext. Data Fig 2) allows us to identify four distinct combinations of incident fundamental and outgoing SHG polarizations that are uniquely sensitive to each of the magnetic states. We were thus able to verify that the current-induced switching in Fig. 3c is between $\mathbf{M}_{\pm y}$ states. In the absence of a magnetic field bias, we can identify an oblique polarization angle, where the intensity of all four magnetic states is different and assign the domains (right hand side). Yellow circles show positions of gold electrodes.

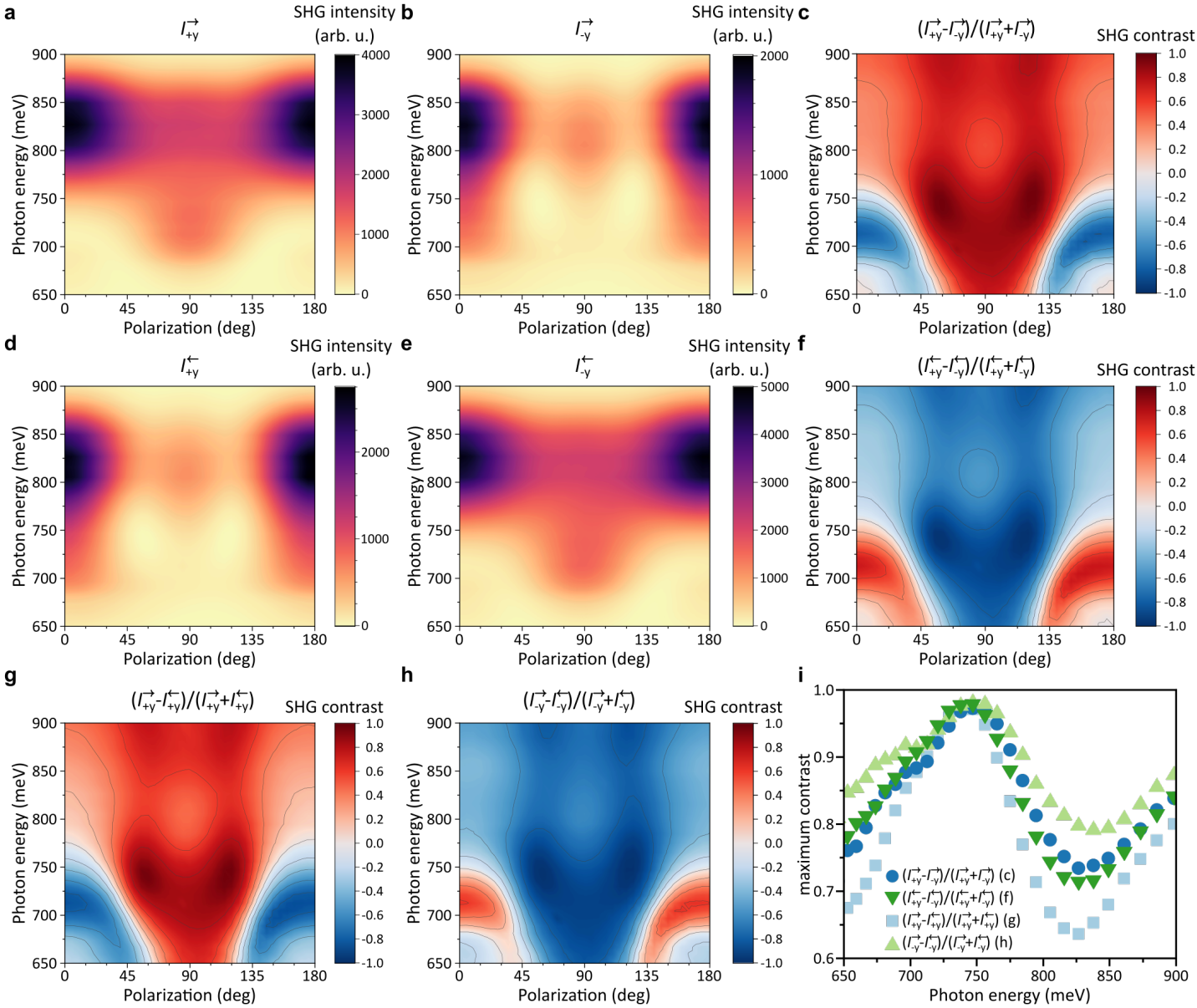

Extendend Data Fig. 6. **Determination and robustness of nonreciprocal contrast (Fig. 4a). a,** 2D map of measured p-polarized SHG intensity in forward direction as a function of incident polarization and photon energy for the $\mathbf{M}_{+y}$ state and **b,** $\mathbf{M}_{-y}$ state. **c,** nonreciprocal contrast η as defined by Eq. (2). **d-f,** analogous to **a-c** in backward direction. **g,h,** nonreciprocal contrast defined as contrast between opposite directions in the same magnetic state. Panels **c**, **f**, **g**, and h are all consistent, demonstrating the robustness of determining the nonreciprocal contrast. **i,** Maximum contrast analogous to Fig. 4b for panels **c**, **f**, **g**, and **h**. Maximum contrast extracted from **c**, **f** agree well, whereas experimental uncertainties in reversing the beam path cause slight deviations between **g** and **h**. The absolute value of panel **c** is shown in Fig. 4a.

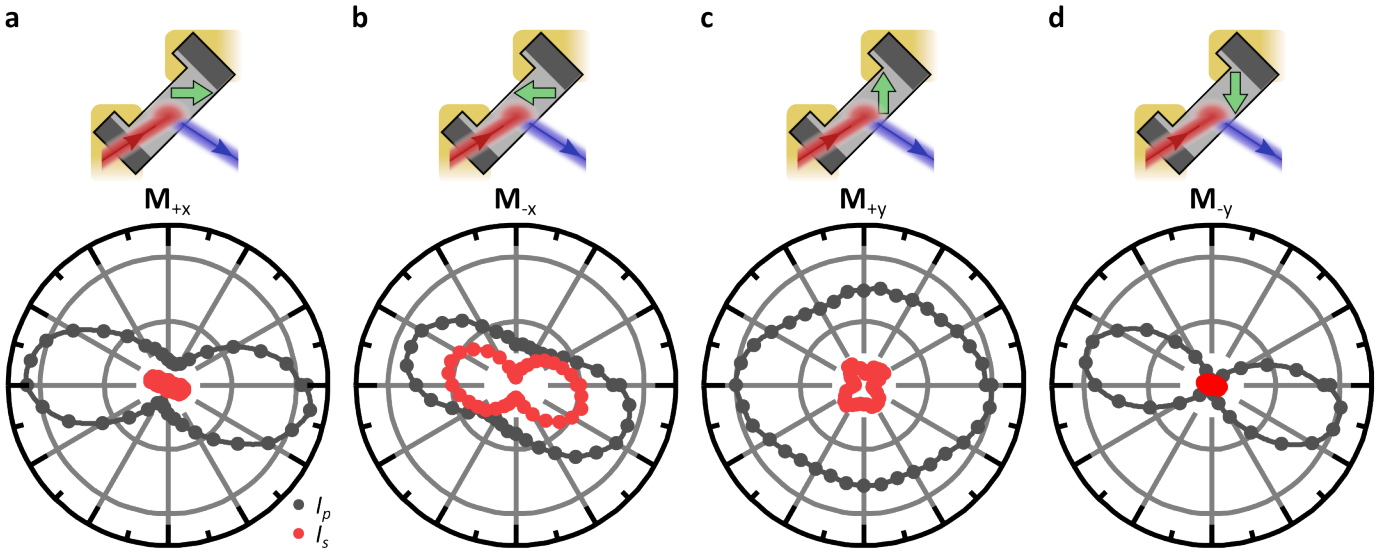

Extendend Data Fig. 7. **SHG Polarization dependencies for FIB-sample.** Analogously to the SHG signal from CeAlSi bulk single crystals (Ext. Data Fig. 2), the SHG polarization dependence allows us to distinguish the four magnetization directions in micro-machined CeAlSi samples. Here, the magnetic state was stabilized by an external magnetic field of 30 mT. A comparison of field-polarized measurements to the field-free measurements shown in Figs. 3h,i reveals electrical switching between $\mathbf{M}_{-x}$ and $\mathbf{M}_{+x}$ states, respectively.

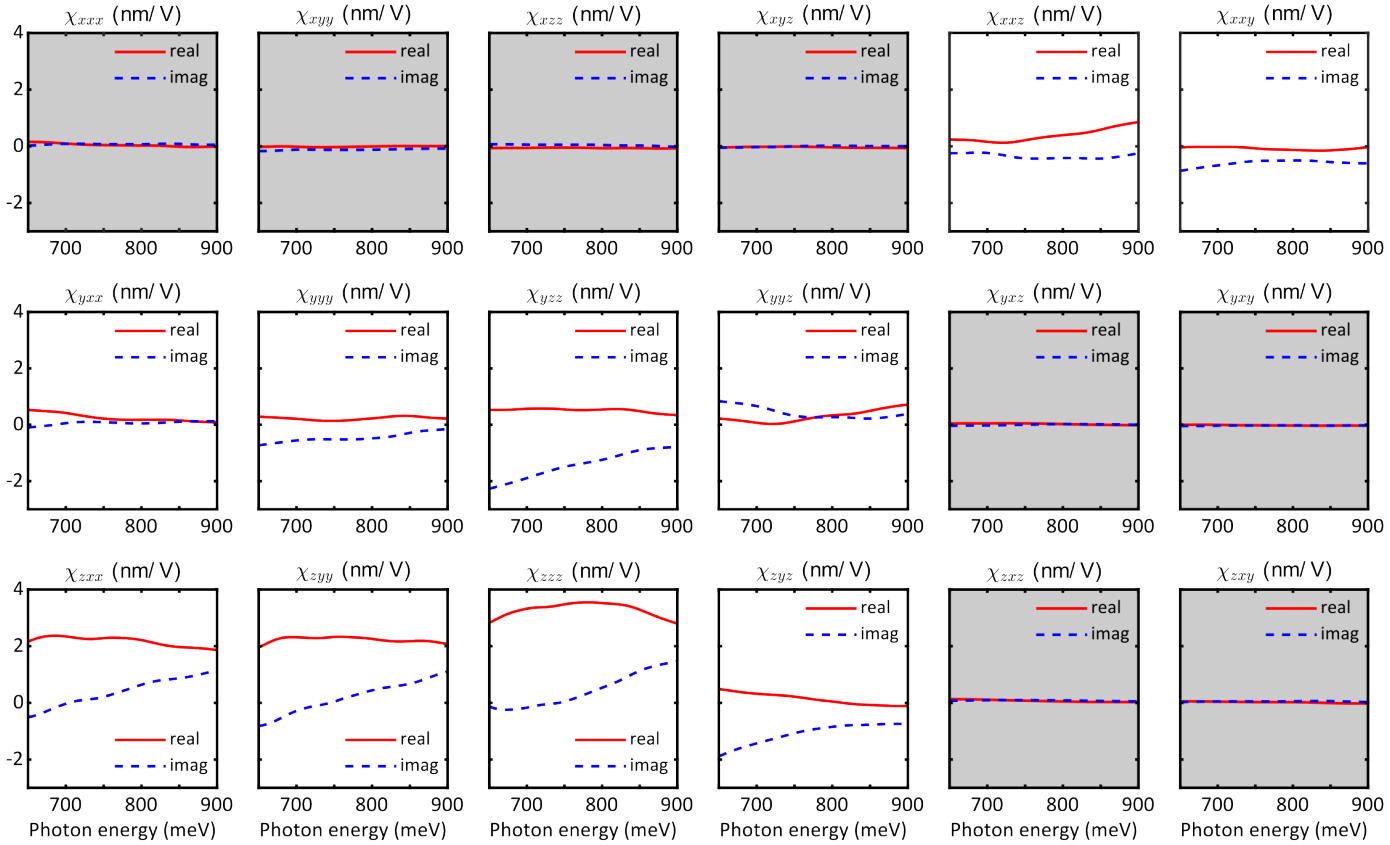

Extendend Data Fig. 8. **First-principles calculations of SHG tensor component spectra in the magnetic phase of CeAlSi.** All spectra are shown on the same scale. In agreement with the $2'mm'$ point group symmetry, the grayed out components vanish. The allowed components evolve continuously without any pronounced resonance in agreement with our understanding of broadband SHG due to linearly dispersive bands in CeAlSi.

ACKNOWLEDGMENT

Work in the SYX group was partly supported through the Center for the Advancement of Topological Semimetals (CATS), an Energy Frontier Research Center (EFRC) funded by the U.S. Department of Energy (DOE) Office of Science (fabrication and measurements), through the Ames National Laboratory under contract DE-AC0207CH11358, and partly by the AFOSR grant FA9550-23-1-0040 (data analysis), and partly by the NSF Career DMR-2143177 (manuscript writing). SYX also acknowledges the Corning Fund for Faculty Development. The work in the QM group was supported through the CATS, an EFRC funded by the DOE Office of Science (manuscript writing), through the Ames National Laboratory under contract DE-AC0207CH11358. QM also acknowledges the support from NSF through a CAREER award DMR-2143426 (material supplies) and the CIFAR Azrieli Global Scholars Program. C.T. acknowledges support from the Swiss National Science Foundation under project no. P2EZP2_191801 and from the Harvard University Climate Change Solutions Fund. J.N. acknowledges support from the Swiss National Science Foundation under project no. P2EZP2_195686. F.H. received funding by the National Natural Science Foundation of China under grant 52103353. P.J.W.M. acknowledges funding by the European Research Council (ERC) under the European Union's Horizon 2020 research and innovation programme (MiTopMat, grant agreement no. 715730). C.G. received funding by the Swiss National Science Foundation (grant no. PP00P2_176789). This material is based upon work supported by the Air Force Office of Scientific Research under award number FA2386-21-1-4059. K.T.L. acknowledges the support of HKRGC through Grants RFS2021-6S03, C6025-19G, AoE/P-701/20, 16310520, 16310219 and 16307622.

AUTHOR CONTRIBUTIONS

C.T. designed and conducted the SHG experiments with assistance from J.-X.Q., H.-C.L., Y.-F.L., A.G., D.B., T.D., and S.-C.H. C.T. evaluated the data with support from J.N. X.-J.G., C.-P.Z., Y.-M.X., and K.T.L. performed the first-principles calculations. H.-Y.Y., X.P., Y.F., F.H., and F.T. synthesized CeAlSi single crystals. C.G. and P.M. prepared the FIB cut. C.T., Q.M. and S.-Y.X. wrote the manuscript with discussions and contributions from all authors.

METHODS

Crystal growth

Single crystals of CeAlSi were grown by a self-flux method. The starting materials were Ce and Al ingots, and Si pieces, mixed in ratio Ce:Al:Si = 1:10:1 in an alumina crucible. The crucible was sealed in an evacuated quartz tube,

and went through the following heating sequence: the sample was heated from 25 °C to 1000 °C at 3 °C min^{-1}, stayed for 12 h, cooled to 700 °C at 0.1 °C min^{-1}, stayed for 12 h, and finally centrifuged to remove the residual Al flux at 700 °C.

SHG measurements

Second-harmonic generation (SHG) is a nonlinear optical process that describes the interaction of two photons at frequency ω in a material leading to the re-emission of one photon at frequency 2ω. In the lowest-order electric-dipole approximation, the process can be formally expressed as

$$P_i(2\omega) = \sum_{j,k} \mathcal{X}_{ijk} E_j(\omega) E_k(\omega), \tag{3}$$

where $E_j(\omega)$ and $E_k(\omega)$ denote the electric-field components of the incident light-wave and P_i the components of the induced nonlinear polarization oscillating at 2ω (indices i, j, k can be x, y, or z). The process is mediated by the second-order susceptibility tensor $\mathcal{X}_{ijk}$, which can only have non-vanishing components when $\mathcal{P}$ is broken[33].

All SHG measurements were obtained using a laser system by LightConversion consisting of an amplified femtosecond laser (Pharos, photon energy 1.2 eV, maximum power 10 W, maximum repetition rate 100 kHz) in combination with an optical parametric amplifier (Orpheus One HE). In order to avoid heating effects, we reduce the repetition rate of the laser and employ attenuating filters to achieve an average power on the sample of less than 2 mW. For domain imaging (e.g., Fig 2i), we chose a spot size of approximately 800 µm. For all other measurements, we focused the laser to a spot size of approximately 150 µm. All SHG measurements were performed in reflection under an angle of incidence of 45°. We adjust the laser polarization of the incident fundamental beam using an achromatic half-waveplate, while selectively detecting s- and p-polarized SHG intensity (red and gray data points, respectively) using a Glan-laser polarizer and a thermo-electrically cooled electron-multiplying CCD camera (EMCCD). For spectrally resolved SHG measurements, a grating spectrometer was mounted in front of the EMCCD camera. For all other measurements, the EMCCD camera was mounted behind a narrow band pass filter centered at 1.425 eV (bandwidth 30 meV). We used additional filters directly before the sample to block parasitic SHG signals from all previous optical components as well as directly after the sample to block the fundamental beam.

The measured SHG intensity is proportional to

$$I(2\omega) = |\mathbf{P}(2\omega) \cdot \mathbf{A}|^2 = |\sum_{i,j,k} \mathcal{X}_{ijk} E_j(\omega) E_k(\omega) A_i|^2, \tag{4}$$

where $\mathbf{A}$ is the direction of the transmitted polarization axis of the analyzer (here s or p polarization).

Fitting of SHG polarization dependencies

The SHG polarization dependencies were fit self-consistently according to Eq. (1). In the magnetically ordered phase, the 16 measurements in Extended Data Fig. 2(a-d,f-i) (four magnetization directions, forward/backward propagation, s/p-polarized SHG) were fit simultaneously by optimizing the amplitude and phase of the allowed SHG tensor components of the $2'mm'$ symmetry. The different magnetization directions were simulated by performing 90° rotations of the SHG tensor about the crystallographic c axis. To account for experimental uncertainties, the fit allowed for slight variations of the sample orientation, i.e., rotations about the surface normal and about the horizontal axis in the lab frame as well as deviations of the angle of incidence from 45°. A consistent fit was achieved with all variations being less than 2°. Similarly, the four measurements in Extended Data Fig. 2(e,j) were fit simultaneously with the allowed SHG tensor components of the paramagnetic $4mm$ symmetry. The fit results are not unique but show consistency with the expected symmetries as well as self-consistency of the different measurements.

Focused-ion-beam microstructuring

An oriented large single crystal of CeAlSi was milled using a Xe-Plasma FIB (Thermofisher Helios PFIB). At 2.5mA, 30kV, first a rectangular bar was milled from the parent crystal (bar length 300mm, width 50mm, height 30mm). This bar was attached with Pt deposition to an in-situ micromanipulator and rotated by 90°, to access the side face of the bar. At this angle, the trapezoidal outer shape and the central bridge were patterned at 500nA, 30kV for coarse and 60nA, 30kV for fine patterning. Furthermore, the outer feet were polished flat at 60nA, 30kV to ensure a flat mating with the substrate. A sapphire substrate (2x2mm) with two large, lithographically prepared Au leads (10nm Ti / 100nm Au) was introduced into the chamber and the bridge rotated back. Using the in-situ manipulator, the bridge was placed ontop of these Au pads and connected by Pt deposition (60nA, 12kV), on the right foot in main Fig. 3f. The tip of the manipulator was cut off (60nA, 30kV), and the remains of the manipulator are well visible on the front section of the right foot. Despite best efforts of alignment, an approximately 500nm gap appeared between the left foot and the Au pad. The micromanipulator was used to gently push the structure flat, yet without forming a solid bond via deposition. Using the same settings as on the right side, the left side was connected with Pt. The sizable depositions resulted in visible overspray, which at these channel lengths does not notably conduct. Out of caution, the overspray was removed in a rectangular channel on both sides of the bridge (60nA, 30kV). The FIB process at 30kV usually results in a 20nm thick amorphous layer which may cause issues with the SHG experiments. This layer was strongly reduced using low-voltage polishing. At an angle of 52° between the beam and the surface normal, the central top of the bridge was irradiated at 60nA, 5kV in a final cleaning step. As the entire process is performed using

Xe beams, no implantation of the primary ions is expected.

First-principles calculations

We performed density-functional theory calculations[44] using the *Vienna Ab initio Simulation Package* (VASP)[45] with the Perdew-Berke-Ernzerhof's (PBE) pseudopotential[46] in the generalized-gradient approximation[47]. We adopted $U_{\text{eff}} = 6\,\text{eV}$ for the Hubbard U-term acting on the Ce f-orbital electrons[22]. The Wannier tight-binding Hamiltonians were established using the *Wannier*90 package[48]. The Wannier bands were symmetrized to restore the symmetry restrictions of the CeAlSi space group[49]. The magnetic order of CeAlSi is described by two magnetic sublattices of equal magnitude with noncollinear magnetic moments $\mathbf{m}_1$ and $\mathbf{m}_2$ on Ce $4f$ orbitals such that $(\mathbf{m}_1 + \mathbf{m}_2) \parallel [110]$. The angle between $\mathbf{m}_1$ and $\mathbf{m}_2$ is 70° as indicated in Ref.[22].

Calculation of χ_{ijk}

We calculated the nonlinear optical susceptibility χ_{ijk} for electric-dipole SHG according to the diagrammatic approach to the nonlinear optical response[50,51]. Interband transitions cause two contributions ξ^I and ξ^{II} such that $\chi_{ijk} = \int_{BZ} d^3\mathbf{k} \left(\xi^I_{ijk} + \xi^{II}_{ijk}\right)$, where

$$\xi^I_{ijk} = C \sum_{m\neq n} f_{mn} \left(\frac{h^{ij}_{nm} h^k_{mn} + h^{ik}_{nm} h^j_{mn}}{\omega + i\eta - \omega_{mn}} + \frac{h^{jk}_{mn} h^i_{nm}}{2\omega + i\eta - \omega_{mn}} \right), \tag{5}$$

$$\xi^{II}_{ijk} = C \sum_{m\neq n\neq p} \frac{h^i_{pm} \left(h^j_{mn} h^k_{np} + h^k_{mn} h^j_{np}\right)}{\omega_{mn} + \omega_{np}} \left(\frac{f_{np}}{\omega + i\eta - \omega_{pn}} + \frac{f_{nm}}{\omega + i\eta - \omega_{nm}} + \frac{2 f_{mp}}{\omega + i\eta - \omega_{pm}} \right) \tag{6}$$

Here, $\{i,j,k\}$ run over $\{x,y,z\}$ directions, $C = \frac{e^3}{2i\epsilon_0 \hbar^2 \omega^3}$, $\{m,n,p\}$ are the band indices, $h^i_{mn} = \frac{1}{\hbar}\langle m|\partial_{k_i} h(\mathbf{k})|n\rangle$, $h^{ij}_{mn} = \frac{1}{\hbar}\langle m|\partial_{k_i}\partial_{k_j} h(\mathbf{k})|n\rangle$, $\omega_{mn} = \frac{1}{\hbar}(\epsilon_m - \epsilon_n)$ represents the transition frequency between bands m and n, f_{mn} is the difference in band occupation according to the Fermi-Dirac distribution, and ϵ_0 is the vacuum permittivity. The derivatives h^i_{mn} and h^{ij}_{mn} can be rewritten in terms of the generalized Berry connection $\mathcal{A}^i_{mn} = i\langle m|\partial_{k_i}|n\rangle$[52]:

$$h^i_{mn} = \frac{1}{\hbar}\langle m|\partial_{k_i} h(\mathbf{k})|n\rangle = \partial_{k_i}\langle m|h(\mathbf{k})|n\rangle - \langle \partial_{k_i} m|h(\mathbf{k})|n\rangle - \langle m|h(\mathbf{k})|\partial_{k_i} n\rangle = \delta_{mn}\partial_{k_i}\epsilon_m + i\hbar\omega_{mn}\mathcal{A}^i_{mn}. \tag{7}$$

As the summation in Eqs. (5) and (6) only considers interband transitions ($m \neq n$), we find $h^i_{mn} = i\hbar\omega_{mn}\mathcal{A}^i_{mn}$. Similarly, we find $h^{ij}_{mn} = i\hbar\mathcal{A}^i_{mn}\partial_{k_j}\omega_{mn}$ for the relevant case of $m \neq n$. Therefore, all interband contributions to χ_{ijk} can be related to the generalized Berry connection $\mathcal{A}^i_{mn}$.

Using $\chi_{ijk} = \int_{BZ} d^3\mathbf{k}\,\xi_{ijk}$ and Eq. (4), we can express the SHG intensity as

$$I(2\omega) = |\int_{BZ} \sum_{i,j,k} \xi_{ijk} E_j(\omega) E_k(\omega) A_i d^3\mathbf{k}|^2 = |\int_{BZ} \kappa d^3\mathbf{k}|^2, \tag{8}$$

where we define $\kappa = \sum_{i,j,k} \xi_{ijk} E_j(\omega) E_k(\omega) A_i$.